



Coupling Graph Attention Networks with Causal Discovery for Geochemical Anomaly Recognition

Zhixiang Liang¹ · Yihui Xiong¹ · Renguang Zuo¹

Received: 19 November 2024 / Accepted: 16 June 2025 / Published online: 21 July 2025
© International Association for Mathematical Geosciences 2025

Abstract

Deep learning methods have achieved notable success in identifying geochemical anomalies. However, these approaches focus primarily on the correlations within the data and have limitations in terms of interpretability, generalization, and robustness. To address these issues, four types of knowledge—logical, visual, scientific, and causal knowledge—can be integrated to enhance data-knowledge-driven deep learning models. This study highlights the role of causal knowledge, specifically in leveraging causal discovery to strengthen model interpretability and robustness. A hybrid model, causal graph attention networks (C-GAT), was developed by integrating the linear non-Gaussian acyclic model (LiNGAM) causal discovery model with a graph attention network (GAT). This integration allows C-GAT to adjust data structures to emphasize causally relevant features, reduce spurious correlations, and improve attention coefficient distribution. In a case study of lithium-beryllium-niobium-tantalum polymetallic deposits in the Nanling region, C-GAT outperformed traditional GAT in terms of accuracy and robustness, effectively identified complex geochemical patterns, and maintained stable performance under varying noise levels. These results highlight the potential of causal relationships to enhance geochemical exploration models by focusing on geologically significant variables.

Keywords Causal discovery · Graph attention network · Geochemical anomaly recognition · Robustness

✉ Yihui Xiong
xiongyh426@cug.edu.cn

¹ State Key Laboratory of Geological Processes and Mineral Resources, China University of Geosciences, Wuhan 430074, China

1 Introduction

The normal abundance of geochemical elements in unmineralized earth materials is commonly referred to as background, while for a geochemical anomaly it is by definition a deviation from the geochemical background (Carranza 2008). The recognition of geochemical anomaly patterns related to mineralization plays an important role in geochemical prospecting, which aims to identify the presence of mineralization (Carranza 2008; Zuo et al. 2019). Geologists have focused on processing geochemical survey data to efficiently assist in identifying geochemical anomalies (Cheng 2012; Zuo et al. 2021). Geochemical patterns commonly show nonlinearity, spatial heterogeneity, and unknown distributions owing to the complexity of geological systems and the diversity of ore-forming processes (Grunsky 2010; Cheng 2012; Agterberg 2014) or complex physical and chemical processes (Cox 2005; Xiong et al. 2023).

Deep learning has strong nonlinear fitting and feature extraction abilities and can deeply mine the complex patterns concealed behind geochemical data and effectively improve the performance of geochemical pattern recognition (LeCun et al. 2015; Zuo et al. 2019). In geochemical anomaly recognition, a deep learning model can perform data analysis, and then provide mapping from input to output to support high-precision feature extraction (Xiong and Zuo 2016; Zuo et al. 2019). Although nonlinear mapping may not be transparent, the extraction and prediction performance of deep learning is generally impressive (Reichstein et al. 2019), achieving significant success in the identification of geochemical anomalies (Zuo et al. 2023, 2024). However, these methods often focus on the correlation relationship in the data, and with further development of the application, their drawbacks gradually begin to appear, facing a series of urgent problems in terms of interpretability, generalization, and robustness (Zuo et al. 2023).

Adding knowledge guidance is an effective way to alleviate the poor robustness, generalizability, and interpretability of deep learning models powered by both data and knowledge, which could promote innovation in computing paradigms (Karpatne et al. 2017; Reichstein et al. 2019). Logical knowledge, visual knowledge, and laws of scientific knowledge and causal knowledge are commonly used to guide data-driven deep learning models and effectively alleviate the above problems (Pearl 2010; Cortez and Embrechts 2013; Pan 2016; Reichstein et al. 2019; Raissi et al. 2019; Jin et al. 2023). Knowledge graphs are an effective way to acquire logical knowledge, as they can integrate multi-source, heterogeneous geoscience big data and drive knowledge discovery through rules and reasoning (Nickel et al. 2015; Hogan et al. 2021). The infusion of logical knowledge and reasoning from knowledge graphs into the workflow of geochemical anomaly recognition and mineral prospectivity mapping can enhance the intelligence level of mineral predictions, driven by expert knowledge (Wang et al. 2024a, b; Yan et al. 2023, 2024). Visualization techniques can provide relatively transparent intermediate processes (such as the extraction and fusion of prospecting information) by visualizing the output of each hidden layer, thereby further enhancing the interpretability of the deep learning model (Cortez and Embrechts 2013; Luo et al. 2022). The laws of scientific knowledge are conclusions derived from specific facts through repeated scientific experiments and observations and are widely accepted by the scientific community, such as Newton's laws and the law of

conservation of mass (Raissi et al. 2019; Wessels et al. 2020). In the field of mineral exploration, the spatial relationships between geological features and mineral deposits provide a nonlinear controlling function (Zuo 2016) that can be adopted as scientific law to design interpretable hidden layers and loss functions (Xiong et al. 2022; Zuo et al. 2023). Causal knowledge can be obtained through causal discovery and inference methods (Pearl 2010). Multiple studies have argued that the poor interpretability, generalizability, and robustness of deep learning methods are partly due to a lack of causal formalism (Schölkopf 2022; Kaddour et al. 2022). Subsequently, there has been a surge in interest in causal deep learning, which is a hybrid of deep learning methods and causal analysis (Luo et al. 2020; Tesch et al. 2023).

Causality is regarded as an efficient tool for improving the interpretability, generalizability, and robustness of deep learning algorithms (Pearl 2010; Sloman and Lagnado 2015; Guo et al. 2020). Traditional deep learning excels at identifying patterns and correlations in large datasets, primarily for predictive tasks. However, causal deep learning goes beyond pattern recognition by attempting to understand the impact of variable changes on outcomes, that is, the causal relationships between variables (Moraffah et al. 2020; Lagemann et al. 2023). For instance, causal thinking has been integrated into data-driven scientific methods to improve process understanding and develop more robust machine learning and statistical models for time series data in the earth and environmental sciences (Runge et al. 2019). The integration of causal discovery and deep learning is a promising approach that offers more stable and trustworthy prediction models (Luo et al. 2020). Iglesias-Suarez et al. (2024) introduced causally informed deep learning methods that combine causal discovery with deep learning to remove spurious correlations and optimize neural network algorithms for climate simulations. Luo and Zuo (2025) demonstrated the application of causal discovery algorithms combined with deep learning models in geochemical exploration, effectively identifying pathfinder elements in complex geochemical datasets and improving anomaly pattern recognition, which is essential for mineral potential mapping.

Among the numerous methods for identifying geochemical anomalies based on deep learning, graph-based models, such as graph neural networks (GNNs), show a remarkable ability to model the nonlinearity and spatial heterogeneity of geochemical patterns due to the flexibility of the graph structure with vertices and edges. This approach, through its adaptable architecture, enables comprehensive characterization of both spatial characteristics and heterogeneity in geochemical data (Gori et al. 2005), offering superior capability for modeling complex geochemical patterns (Guan et al. 2022). For example, Guan et al. (2022) proposed an unsupervised learning framework that adopts a combination of a graph attention network (GAT) and an autoencoder for mapping geochemical anomalies. Xu et al. (2023) employed GAT to identify geochemical anomalies associated with gold mineralization, and further explain the geochemical element contribution of GAT based on GNNExplainer, revealing elements strongly related to known gold mineralization. All the aforementioned studies demonstrate that GAT has great potential in mining geochemical data. However, as a deep learning model, GAT also faces issues in the aspects of interpretability and robustness.

In this study, a causal discovery method, the linear non-Gaussian acyclic model (LiNGAM) (Shimizu et al. 2006), in which the error variables are assumed to follow

non-Gaussian continuous distributions, was adopted to mine the causal relationship between geochemical variables and mineralization in order to enhance the interpretability and robustness of GAT for geochemical anomaly recognition. Several recent studies have combined causal discovery methods with GAT to improve robustness and interpretability in various tasks. For instance, Sui et al. (2022) proposed a causal attention mechanism tailored for graph classification, addressing confounding effects to enhance generalization on out-of-distribution data. Liu et al. (2023) developed a causal graph attention model with disentangled representations aimed at fault detection in complex systems. Building on previous works, we combine LiNGAM and GAT, namely the causal graph attention network (C-GAT), to further address the challenges of interpretability and robustness in deep learning-based geochemical anomaly identification. For interpretability, causal discovery algorithms (e.g., LiNGAM) can uncover the causal relationships between geochemical variables and mineralization, which provides indicative meaning for geochemical anomaly identification. For robustness, deep learning models are fragile and can completely change their predictions when the input data are disturbed, even if these perturbations are imperceptible (Goodfellow et al. 2014; Carlini and Wagner 2017). These data disturbance problems caused by noise and incomplete data pose challenges for the application of deep learning in geochemical anomaly recognition (Xiong et al. 2022). Specifically, graph neural networks may be affected by perturbations in graph data, which can disrupt node information and attention coefficients (Geisler et al. 2021; Mujkanovic et al. 2022). This causal relationship obtained by LiNGAM can be used to update the attention coefficients of the GAT to uncover spurious correlations in data, and by removing these spurious correlations, the robustness of the model to data perturbations can be improved (Schölkopf 2022; Kaddour et al. 2022).

2 Geological Setting and Datasets

2.1 Geological Setting

The Nanling region is a major ore concentration area for lithium, beryllium, niobium, and tantalum polymetallic mineralization belt in China and spans several provinces, including Jiangxi, Hunan, and Guangdong. The deposits in this district (Fig. 1) are often found together with other deposits and are predominantly granite-type lithium-beryllium-niobium-tantalum deposits (Zhao et al. 2022). During the Caledonian Orogeny, the Cathaysian Plate collided with the Yangzi Plate, forming a continental mass (Yang et al. 1997), which positioned the Nanling region at the suture zone between these two plates. Because of this unique geotectonic setting, the Nanling region has undergone considerable tectonic–magmatic activity (Wang et al. 2003; Xuan et al. 2014), resulting in the exposure of three phases of granites: Caledonian, Indosian, and Yanshanian. The Yanshanian granites account for approximately 30% of the total granite in the region (Zhou et al. 2006).

The Indosian granites were primarily formed in syn-collisional and post-collisional geodynamic environments (Chen and Jahn 1998; Hua et al. 2005). Notable examples include the Toupi lithium-beryllium-niobium-tantalum deposits in

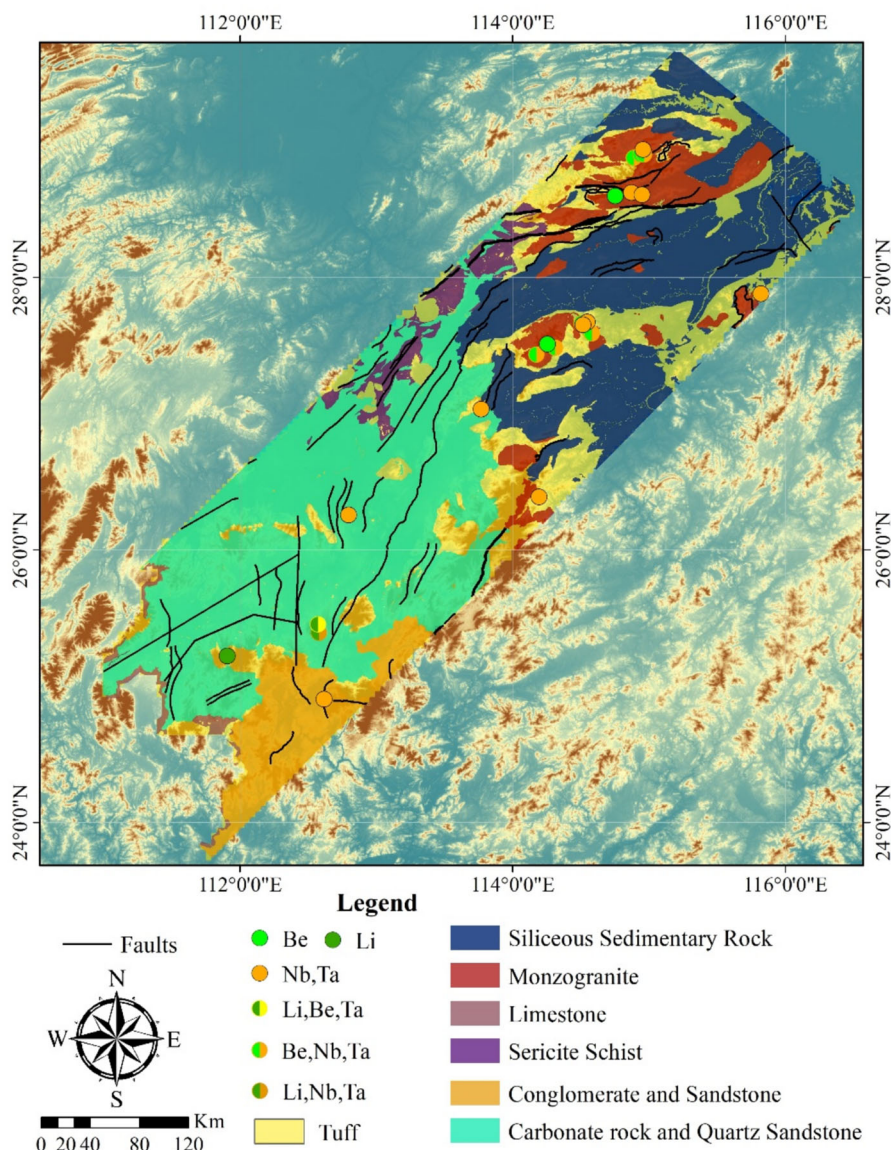


Fig. 1 Simplified geological setting of the Nanling region in Southern China (modified from Zhou et al. 2006)

Guangchang county, Jiangxi Province (~246 Ma, Che et al. 2019), and the Heyuan lithium-beryllium-niobium-tantalum deposits in Heyuan county, Guangdong Province (~200 Ma, Hu and Huang 2005). In contrast, magmatic activity during the Yanshanian period (Jurassic to Cretaceous) occurred over a short period of 165–155 Ma, leading to the widespread distribution of large-scale granite bodies (Li et al. 2007).

The lithium-beryllium-niobium-tantalum deposits in Jianfengling, Hunan Province (~158 Ma, Wen et al. 2017, 2021) are the most representative deposits. Notably, the strike of the Nanling granite belt generally aligns with the Nanling mountain range, exhibiting an east–west belt distribution (Chen et al. 2002). Its lithology is mainly alkali-rich, Fe–Mg-poor, strongly peraluminous diorite granite, often accompanied by pegmatites and tourmaline-rich minerals (Qiao et al. 2015; Liu et al. 2019).

From a tectonic perspective, the Nanling region, an important overlapping area between the paleo-tethys ocean and maritime pacific ocean tectonic domain, became a favorable site for mineralization following the closure of the paleo-tethys ocean. Metamorphic dome structures formed by continent-continent collisions provide conducive conditions for mineralization. Mineralizing materials mainly originate from marine sediments between the plates (Xu et al. 2018); consequently, most ore bodies in the study area are located in the anticlines of fold systems (Zhao 2022).

2.2 Datasets

Geochemical data for the study area were obtained from the Chinese national geochemical mapping project. In areas that were difficult to access, the sampling density was lower (one sample per 20–50 km²), whereas in areas that were easier to access, it was higher (one sample per 4 km²). These datasets include the concentrations of 39 major and trace geochemical elements, which have contributed significantly to the discovery of numerous mineral deposits in recent years (Xie et al. 1997; Xi and Li 2017). Geochemical data processing via big data analysis not only can focus on elements related to mineralization but also can incorporate other elements available to map geochemical signatures associated with mineralization (Zuo and Xiong 2018; Xiong et al. 2018). Consequently, all 39 geochemical elements in this study were used to model causal relationships. These geochemical indicators serve as direct evidence of lithium-beryllium-niobium-tantalum polymetallic deposits in this area. Thus, 39 geochemical elements were used to identify the geochemical patterns (Xiong and Zuo 2021).

3 Methods

Conventional graph neural networks typically employ a fixed weight assignment strategy to process for graph structures. To improve the model's performance in handling heterogeneous graphs and complex graph structures, the attention mechanism was introduced, leading to the development of the graph attention network (GAT) (Velicković et al. 2018). This model adaptively assigns weights to the nodes, providing a more precise representation of the interactions between them. However, when noise or perturbations affect the nodes in the GAT model, the classification accuracy may decrease significantly, because the model's reliance on spatial adjacency makes it susceptible to such disturbances. To address this, we incorporated a causal discovery step before the training phase. By constructing a causal graph, we can identify and eliminate pseudo-correlations, that is, spurious relationships between variables that

do not reflect true causal interactions, thereby removing misleading associations that could negatively affect the model's ability to learn meaningful patterns. This process improves the robustness of the model against data perturbations by ensuring that it focuses on genuine, causally relevant features rather than on noise or spurious correlations present in the data.

3.1 Graph Attention Networks

In this study, the graph structure was constructed based on the sampling points, with each node's features representing geochemical measurements at the sampling location. The graph attention network (GAT) is a neural network architecture designed to process graph-structured data, first proposed by Veličković et al. (2018). This model addresses the challenge faced by conventional graph neural networks in assigning different weights to neighboring nodes by introducing a self-attention mechanism (Kipf et al. 2016). In the GAT, attention coefficients are computed and used to weigh and aggregate information from neighboring nodes for the target node, thereby enhancing the model's expressive power (Han et al. 2021; Wang et al. 2022). This transformation is achieved using a weight matrix $W \in R^{F' \times F}$, where F is the number of features of each node, and F' is the dimension of the transformed features.

First, the model applies a linear transformation to each node feature and computes the relevance between the neighboring nodes. The importance of node j to node i (the attention coefficient) is calculated as

$$e_{ij} = \text{LeakyReLU}\left(\overrightarrow{\alpha}^T [W \vec{h}_i \| W \vec{h}_j]\right), \quad (1)$$

where e_{ij} denotes the importance of the features of node j to node i , \vec{h} is the set of node features, and $\overrightarrow{\alpha}$ is a shared learnable weight vector used to measure the interactions between pairs of node features. The attention coefficient was parameterized by a single-layer feed-forward neural network using LeakyReLU nonlinearity with a negative slope of 0.2.

Then, e_{ij} is normalized using the softmax function to obtain the final attention coefficient α_{ij}

$$\alpha_{ij} = \text{softmax}(e_{ij}) = \frac{\exp\left(\text{LeakyReLU}\left(\overrightarrow{\alpha}^T [W \vec{h}_i \| W \vec{h}_j]\right)\right)}{\sum_{k \in \mathcal{N}_i} \exp\left(\text{LeakyReLU}\left(\overrightarrow{\alpha}^T [W \vec{h}_i \| W \vec{h}_k]\right)\right)}, \quad (2)$$

where \mathcal{N}_i denotes the set of neighboring nodes of node i . The normalized attention coefficient α_{ij} serves as the weight for neighboring nodes information, enabling the weighted aggregation of node information to compute the features of the next layer. In this model, the node information is aggregated by explicitly using the attention coefficients as weights for the neighboring node features. The updated feature \vec{h}_i^l in layer l is computed by aggregating the weighted features of the neighboring nodes as

shown in Eq. (3), followed by the application of an activation function

$$\vec{h}_i^l = \text{ReLU} \left(\sum_{k \in \mathcal{N}_i} \alpha_{ik} \vec{h}_k^{l-1} \right). \quad (3)$$

Here, $\text{ReLU}(\bullet)$ denotes the ReLU activation function, which introduces nonlinearity to the model, and \vec{h}_k^{l-1} represents the node features of the $(l-1)^{\text{th}}$ layer. When $l=1$, the \vec{h}_k^{l-1} denotes a preliminary node feature.

3.2 Causal Graph Attention Network (C-GAT)

Noise is often introduced into geochemical data during sampling, preprocessing, and analysis (Pei and Bao 1998). In the GAT, when a node is affected by perturbations (i.e., noise), the disturbance not only impacts the node itself but also propagates to neighboring nodes. This propagation disrupts the importance between nodes and alters the attention coefficient α . Consequently, these perturbations affect the classification performance of the GAT and reduce the model's robustness (Zhang et al. 2023). Causal methods have long been recognized as an effective approach to improve the robustness of machine learning (Pearl 2000). To address this issue, we incorporate causal methods into the GAT to identify genuine relationships among variables and filter out misleading associations in the data, thereby enhancing the robustness of the model (Fig. 2). Specifically, compared with the conventional GAT workflow, the proposed C-GAT model introduces an additional causal discovery step using the LiNGAM. This causal discovery step identifies causal relationships among geochemical variables,

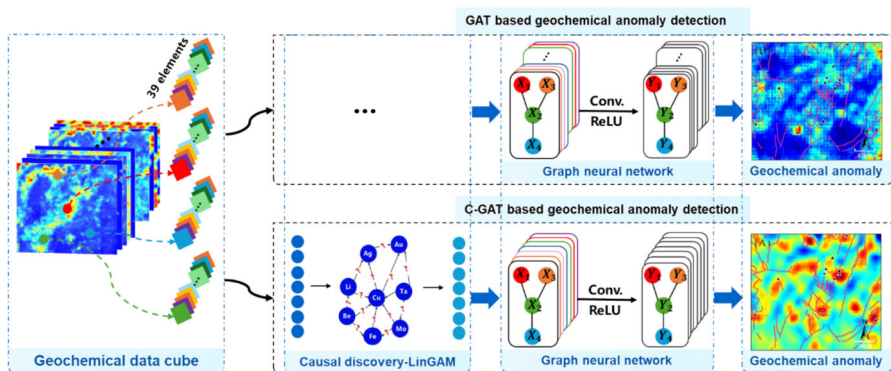


Fig. 2 Comparison of workflows between the conventional graph attention network (GAT) and the proposed causal graph attention network (C-GAT). The upper and lower rows show the GAT- and C-GAT-based geochemical anomaly detection procedures, respectively. Compared with the conventional GAT workflow, the proposed C-GAT model introduces an additional causal discovery step using the LiNGAM. This causal discovery step identifies causal relationships among geochemical variables, producing a causal weight matrix that is subsequently used to adjust node features

producing a causal weight matrix that is subsequently used to adjust node features. Such causal adjustments explicitly enhance the attention mechanism on geologically meaningful variables, thereby improving model interpretability and robustness against data perturbations.

Nodes and edges are the two important attributes of a graph. In this study, edges were constructed between the geochemical sampling points based on Tobler's first law of geography (Tobler 1970), which states that everything is related to everything else, but near things are more related than distant things. Thus, neighboring sampling points are expected to have stronger relationships in the constructed graph. Additionally, the initial feature information of the nodes at the geochemical sampling points was preprocessed using a causal attribution algorithm, ensuring that the features of these points conformed to intrinsic causal relationships.

After applying causal discovery, we adjust the data to better align with the identified causal structure, which enhances the effectiveness of the attention mechanism in the C-GAT. This adjustment does not directly replace spatial adjacency relations with causal relationships. Instead, it modifies the data to emphasize causally relevant connections, thereby guiding the attention mechanism to focus on features that reflect meaningful causal associations. Through this cause-driven data adjustment, the attention distribution in the C-GAT was refined to prioritize geochemically relevant nodes and edges, improving the model's interpretability, accuracy, and robustness by mitigating the effects of noise and reducing pseudo-correlations.

The causal algorithm used in this study was the linear non-Gaussian acyclic model (LiNGAM), a causal function modeling method proposed by Shimizu et al. (2006, 2014). This method identifies causal relationships based on causal asymmetry (Peters 2017) and independent component analysis (ICA) (Altman and Krzywinski 2015). The method follows the following basic principles:

- (1) Directed acyclic graphs: The observed variables are causally ranked in a certain order in which the cause variable must precede the effect variable, that is, the causal model graphs of the variables must be directed acyclic graphs (DAGs).
- (2) Model a linear and noise term-independent non-Gaussian: The variable χ_i is represented as a linear summation of its corresponding cause variables plus a noise term e_i and a constant c_i , which can be expressed as

$$\chi_i = \sum_{k(j) < k(i)} b_{ij} \chi_j + e_i + c_i, \quad (4)$$

where i and j represent specific variables within the model, and $k(i)$ indicates that the causal rank or ordering of variable χ_j is causally prior to χ_i , meaning that χ_j directly influences χ_i . The coefficient b_{ij} represents the direct causal influence strength from variable j to variable i , as determined by the LiNGAM algorithm. The noise terms e_i are independent of each other and follow a non-Gaussian distribution, which is a key assumption in LiNGAM that allows for a unique solution for the causal model.

Next, we transform the above equation; by preprocessing, we can eliminate the mean value of each χ , eliminate the constant term c_i , and represent it using the matrix

form

$$\chi = B\chi + e, \quad (5)$$

where B is the matrix representing the causal weights, which becomes a lower-triangular matrix with zero diagonal after ordering the variables. Solving for χ at this point yields

$$\chi = (I - B)^{-1}e. \quad (6)$$

Here, I denotes the identity matrix, which has the shape of $F \times F$, and χ is the observed sample feature matrix. Positive and negative samples with 39 geochemical features were selected as the observed samples to calculate the causal weight matrix. By combining the properties of the weight matrix as a strict lower triangle, we can obtain the causal order and the corresponding causal map using methods such as rank substitution. A causal weight matrix was used to further process the geochemical survey data to obtain new preliminary node features in the GAT.

Specifically, given the causal weight matrix B , each entry b_{ij} quantifies the direct causal influence from node j (cause node) to node i (effect node). As noted earlier, the matrix B has a strictly lower-triangular structure after causal ordering. The causal-adjusted feature vector $\vec{x}_{adjusted}$ for each sampling point is computed as

$$\vec{x}_{adjusted} = B\vec{x}. \quad (7)$$

This causal-based adjustment explicitly reconstructs each node's features as linear combinations of its causal parent nodes. Thus, features influenced by strong causal relationships become more prominent, while features with weak or no causal connections are significantly diminished, effectively mitigating the impact of spurious correlations in subsequent modeling steps.

4 Results and Discussion

The graph attention network (GAT) model used here is a supervised learning algorithm that requires labeled positive and negative samples for training. For supervised learning tasks in geochemical anomaly recognition, selecting known mineral deposit locations as positive samples and non-mineralized locations as negative samples ensures that the model effectively identifies mineralization-induced geochemical anomalies while ignoring anomalies caused by other unrelated factors.

For positive samples, we selected lithium-beryllium-niobium-tantalum polymetallic deposits in the region (a total of 24). To ensure a balance between positive and negative samples, we selected 24 negative samples. Negative samples were specifically chosen from areas clearly distant from both known deposits and geological features favorable for mineralization. This strategic selection ensures the validity and effectiveness of negative samples, clearly representing background geochemical conditions rather than anomalous signatures. Commonly used methods for selecting

negative samples include random sampling, using known locations without mineralization, or selecting drill sites where no mineralization has been found (Nykanen et al. 2015). Based on these rules, 24 negative samples were selected among areas distant from favorable mineralization zones. The distribution of the data and positive sample points is illustrated taking the concentration of lithium as an example (Fig. 3).

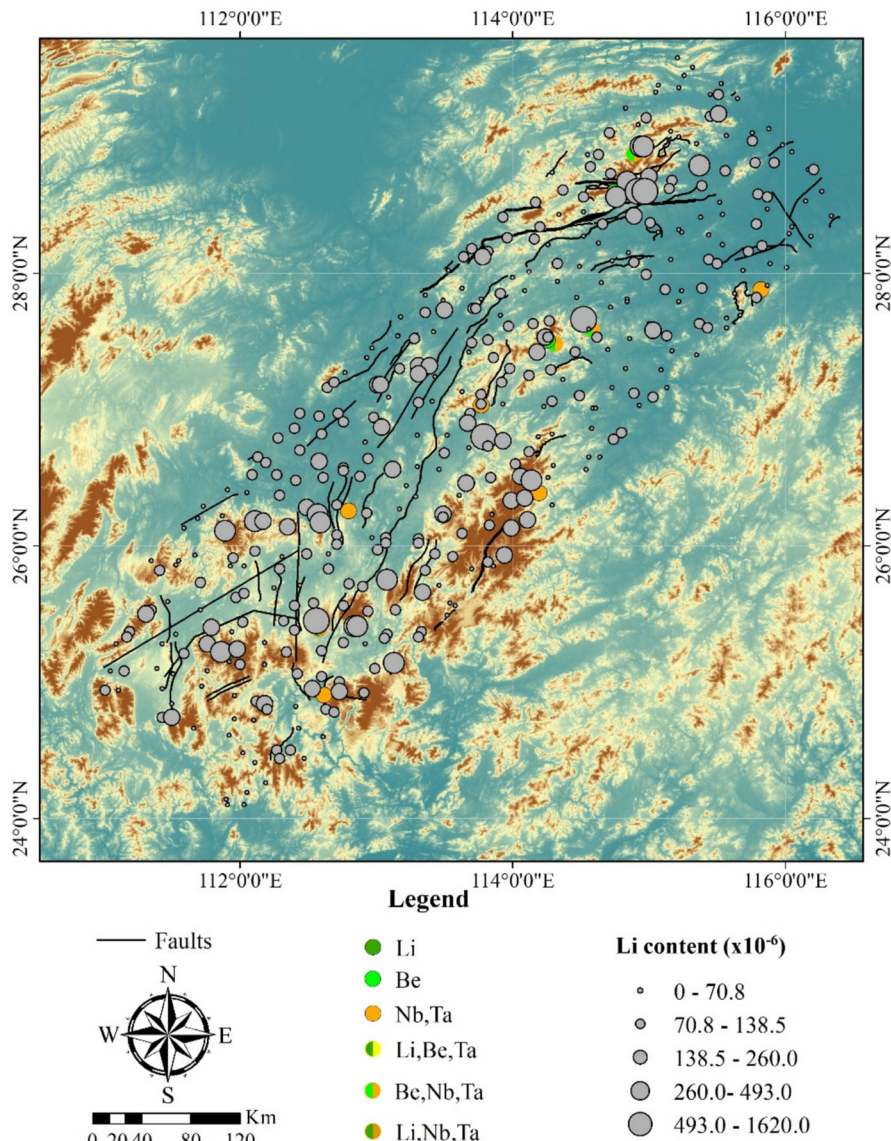


Fig. 3 Visualization of the concentration of the lithium element

4.1 Causal Discovery Between Variables

In this study, the LiNGAM causal algorithm was used to identify causal relationships among 39 elements in the data, constructing a structured representation of elemental interactions relevant to mineralization processes. However, to enhance visual clarity and interpretability, as well as to facilitate rapid verification against established geological knowledge, a simplified causal graph (Fig. 4) was generated by filtering out weaker causal relationships using a threshold of 0.05. This threshold was determined empirically by examining the causal weight distribution obtained from the LiNGAM analysis, and effectively distinguishes meaningful geological interactions from negligible correlations. Nevertheless, it should be emphasized that the complete causal weight matrix actually employed for data adjustment within the C-GAT model captures the comprehensive interactions among all 39 elements to ensure no meaningful causal information is discarded. The arrows in the graph indicate the direction of causality, and each connection represents a causal weight between two variables. Notably, the causal graph shown in Fig. 4, while simplified by filtering weak causal links for clarity, still includes all 39 elements analyzed in this study. Moreover, based on the requirement of clearly illustrating the specific elemental interactions associated with lithium mineralization, we further selected a smaller subset of variables closely related to lithium, resulting in an even more simplified causal graph specifically related to lithium (Fig. 5). In alignment with the established geological knowledge, elements such as K₂O, Al₂O₃, and Li, which are typically associated with granite composition, exhibit strong causal links in the causal graph. Granites in the Nanling region, known for their alkali-rich, Fe–Mg poor composition, serve as host rocks that enrich these elements, particularly during late-stage magmatic differentiation (Qiao et al. 2015; Liu et al. 2019). This causal structure aligns well with the mineralization processes that produce lithium–beryllium–niobium–tantalum polymetallic deposits, supporting the geological consistency of the causal discovery.

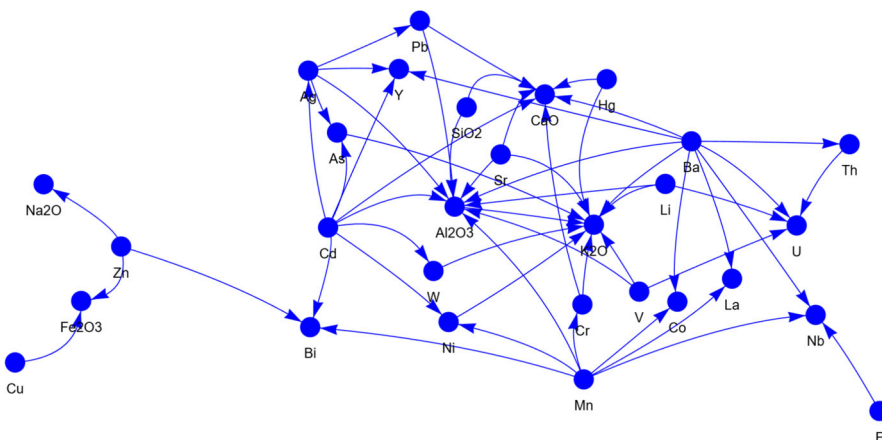


Fig. 4 Causal diagram with full geochemical elements

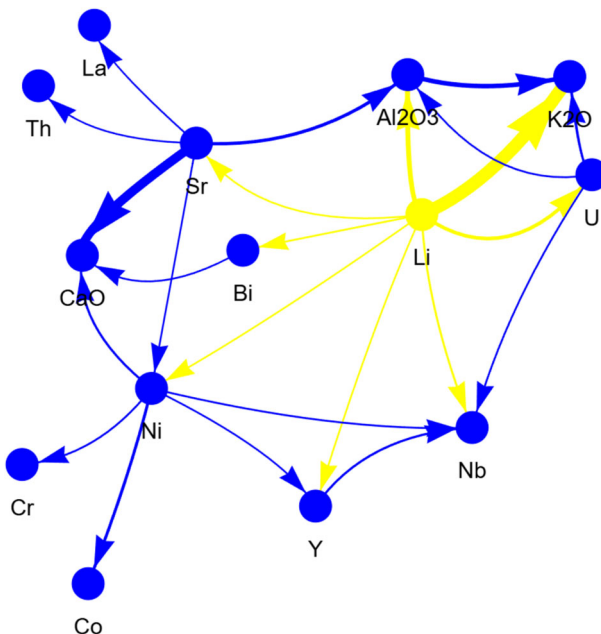


Fig. 5 Li-related geochemical element causal diagram. The yellow arrows represent a direct causal relationship with the ore-forming element Li, while the blue arrows represent an indirect causal relationship with the ore-forming element Li. The thickness of these arrows indicates the strength of the causal relationship: the thicker the arrow, the stronger the causal relationship; conversely, the thinner the arrow, the weaker the causal relationship

The attention scores presented in Table 1 were derived from the node-level attention mechanism of the C-GAT model. Specifically, these scores quantify the relative importance the model assigns to each geochemical element based on aggregated attention weights from multiple graph attention network (GAT) layers. Higher attention scores indicate a stronger influence of the corresponding elements in predicting geochemical anomalies, reflecting their relevance to ore-forming processes. Thus, changes in attention scores before and after causal adjustment illustrate how the causal integration directs the model's focus towards more geologically meaningful elements.

The effect of this causal structure is evident in the attention distribution of the C-GAT model (Table 1). Despite the slight decrease in the overall average attention score from 65.65 to 64.92 after causal adjustment, several elements relevant to lithium polymetallic mineralization exhibited significant relative percentage increases in their attention shares. Specifically, common polymetallic elements associated with lithium deposits, including Li (+1.21%), Be (+1.41%), and Nb (+0.61%), demonstrated meaningful relative increases. Additionally, Bi (+5.30%) and Pb (+3.52%), two widely recognized associated elements frequently found alongside lithium mineralization, displayed substantial relative increases. Furthermore, K₂O (+1.01%), a well-known geochemical indicator closely linked to granite-related mineralization processes, also showed a clear relative increase. Conversely, for elements with weaker causal links,

Table 1 Attention scores, shares, and changes before and after adjustment

| Element | Attention score (unadjusted) | Attention share (unadjusted) | Attention score (adjusted) | Attention share (adjusted) | Relative change (%) |
|--------------------------------|---------------------------------|---------------------------------|----------------------------------|----------------------------------|------------------------|
| F | 95.89 | 3.74% | 84.05 | 3.32% | -11.23% |
| Zn | 85.89 | 3.35% | 79.63 | 3.14% | -6.27% |
| Ni | 86.42 | 3.38% | 83.18 | 3.29% | -2.66% |
| Mo | 87.95 | 3.44% | 85.54 | 3.38% | -1.74% |
| Ba | 82.85 | 3.24% | 80.8 | 3.19% | -1.54% |
| Na ₂ O | 88.48 | 3.46% | 86.33 | 3.41% | -1.45% |
| Al ₂ O ₃ | 44 | 1.72% | 43.15 | 1.70% | -1.16% |
| Ti | 85.05 | 3.32% | 83.58 | 3.30% | -0.60% |
| Hg | 85.71 | 3.35% | 84.29 | 3.33% | -0.60% |
| Cr | 63.76 | 2.49% | 62.82 | 2.48% | -0.40% |
| Y | 63.78 | 2.49% | 63.05 | 2.49% | 0.00% |
| Cd | 85.1 | 3.32% | 84.3 | 3.33% | 0.30% |
| Zr | 80.08 | 3.13% | 79.6 | 3.14% | 0.32% |
| Ag | 64.46 | 2.52% | 64.09 | 2.53% | 0.40% |
| Sb | 58.03 | 2.27% | 57.82 | 2.28% | 0.44% |
| Nb | 41.75 | 1.63% | 41.56 | 1.64% | 0.61% |
| Sn | 41.59 | 1.62% | 41.26 | 1.63% | 0.62% |
| Mn | 78.97 | 3.08% | 78.46 | 3.10% | 0.65% |
| Co | 55.26 | 2.16% | 55.15 | 2.18% | 0.93% |
| W | 52.02 | 2.03% | 51.98 | 2.05% | 0.99% |
| K ₂ O | 50.69 | 1.98% | 50.6 | 2.00% | 1.01% |
| CaO | 47.09 | 1.84% | 47.17 | 1.86% | 1.09% |
| V | 45.21 | 1.77% | 45.41 | 1.79% | 1.13% |
| SiO ₂ | 44.78 | 1.75% | 44.71 | 1.77% | 1.14% |
| La | 65.36 | 2.55% | 65.22 | 2.58% | 1.18% |
| MgO | 64.21 | 2.51% | 64.25 | 2.54% | 1.20% |
| Li | 84.47 | 3.30% | 84.69 | 3.34% | 1.21% |
| Cu | 59.89 | 2.34% | 59.9 | 2.37% | 1.28% |
| B | 36.82 | 1.44% | 37.03 | 1.46% | 1.39% |
| Be | 72.71 | 2.84% | 72.96 | 2.88% | 1.41% |
| Fe ₂ O ₃ | 68.66 | 2.68% | 68.85 | 2.72% | 1.49% |
| U | 51.3 | 2.00% | 51.31 | 2.03% | 1.50% |
| Sr | 69.07 | 2.70% | 69.6 | 2.75% | 1.85% |
| As | 66.51 | 2.60% | 66.97 | 2.65% | 1.92% |
| Au | 49.78 | 1.94% | 50.13 | 1.98% | 2.06% |
| Th | 49.54 | 1.93% | 49.93 | 1.97% | 2.07% |

Table 1 (continued)

| Element | Attention score (unadjusted) | Attention share (unadjusted) | Attention score (adjusted) | Attention share (adjusted) | Relative change (%) |
|-------------------------------|---------------------------------|---------------------------------|----------------------------------|----------------------------------|------------------------|
| P | 59.42 | 2.32% | 59.97 | 2.37% | 2.16% |
| Pb | 65.59 | 2.56% | 67.04 | 2.65% | 3.52% |
| Bi | 82.32 | 3.21% | 85.64 | 3.38% | 5.30% |
| Average attention score | 65.65 | — | 64.92 | — | — |

such as F and Zn, a reduction in attention allocation was observed, with F experiencing a particularly marked relative decrease of 11.23%, and Zn showing a notable relative decrease of 6.27%. This reduction in attention allocation for weaker causal elements clearly demonstrates the effectiveness of causal adjustments in reducing the model's susceptibility to irrelevant or spurious correlations.

On a broader scale, the overall attention allocated across all elements decreased slightly after causal adjustment; however, attention scores of most causally relevant elements increased, indicating that the model now concentrates more effectively on elements strongly associated with mineralization processes. This outcome aligns with the findings of Schölkopf et al. (2021) and Runge et al. (2019), who showed that causal adjustments in attention mechanisms can improve model interpretability by reducing attention to nonessential features.

4.2 Geochemical Anomaly Identification

The constructed C-GAT was used to identify geochemical anomalies related to lithium-beryllium-niobium-tantalum mineralization. It is evident that the C-GAT model demonstrates good predictive capabilities, because zones with high anomaly scores are distributed around each known lithium-beryllium-niobium-tantalum polymetallic deposit (Fig. 6a). Compared with the anomalies extracted by GAT, the anomalies extracted by C-GAT further narrow the anomalous areas around known ore deposits (such as Zone 1 and Zone 2), while detecting new anomalies around mineralization-favorable rock masses in previously ore-barren regions (such as Zone 3 and Zone 4). This demonstrates the model's high precision and effectiveness (Fig. 6b). Subsequent performance evaluation metrics (Figs. 7 and 8) also support this conclusion. Moreover, in the central study area around Wufengxian and Dayi, C-GAT delineates more continuous areas with high anomaly scores, which correspond closely to local geological features such as faults and granitoids. Additionally, in the middle-southern Qitianling region, C-GAT identifies a distinct area with high anomaly scores not detected by GAT, and this anomaly closely matches the known geological elements in the region. In addition, the mineralization in this district is closely related to granitoids (Zhang et al.

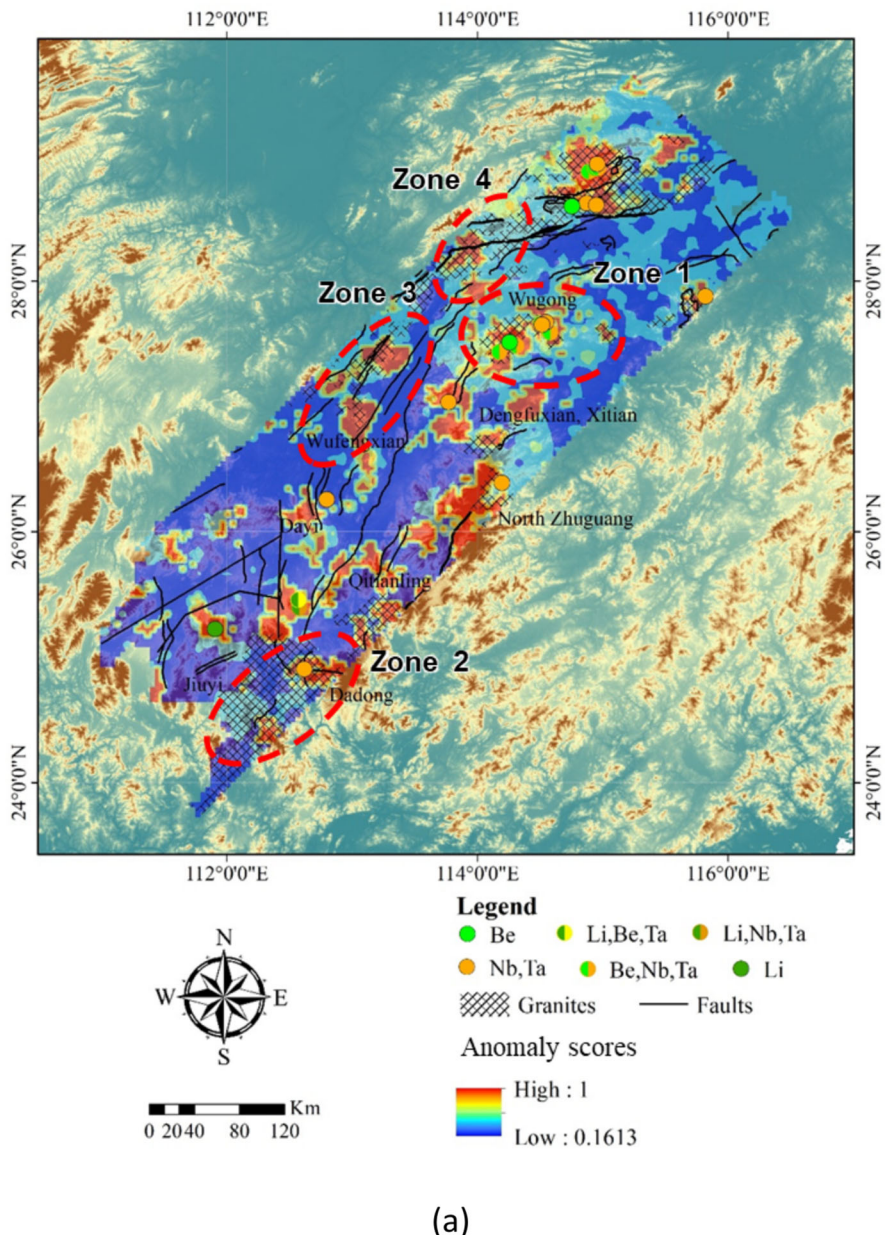


Fig. 6 Geochemical anomaly map identified by **a** C-GAT and **b** GAT

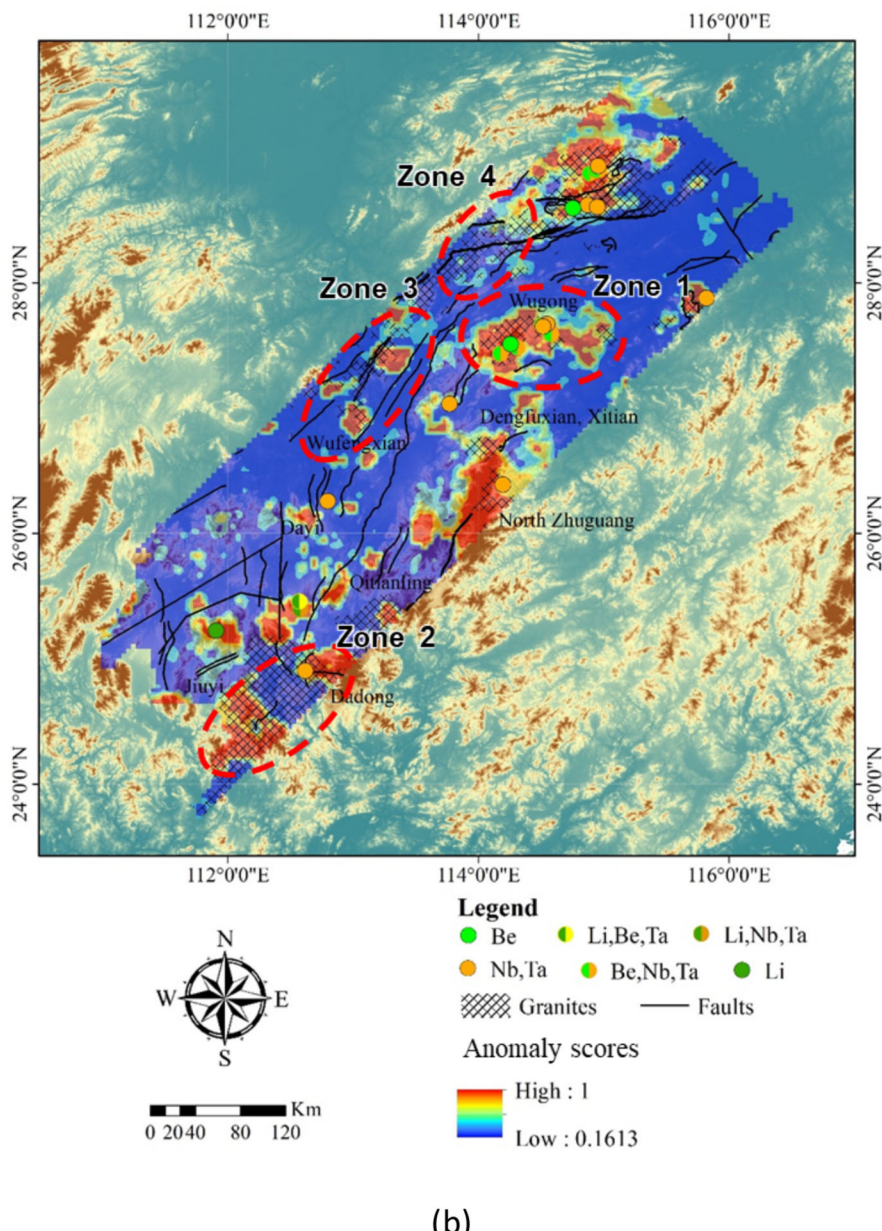


Fig. 6 continued

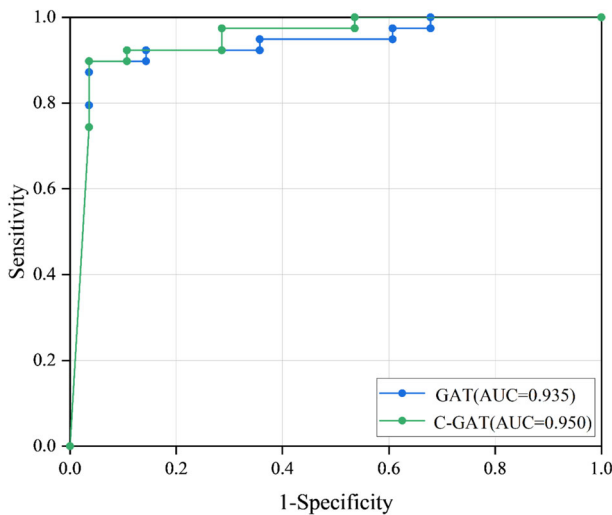


Fig. 7 Comparison of ROC curves of C-GAT and GAT

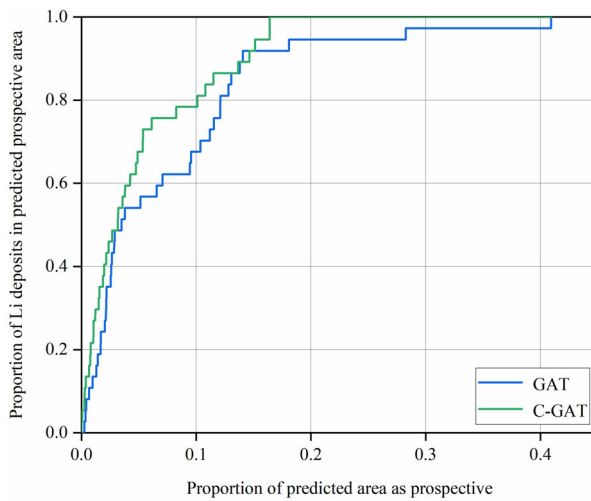


Fig. 8 Success rate curves comparing the performance of C-GAT and GAT models

2012). The spatial analysis results show the spatial relationship between extracted geochemical anomalies and known granitoids, including the Wugong, Dengfuxian, and Xitian granitoids. These results effectively verify the extracted geochemical anomalies. From the receiver operating characteristic (ROC) curve analysis (Fig. 7), C-GAT also outperformed the GAT model, with an area under the curve (AUC) value of 0.95 compared with 0.935 for GAT. This further validated the superiority of the C-GAT

model for geochemical anomaly identification. In summary, C-GAT exhibits a significant advantage over GAT in terms of precision for identifying geochemical anomalies, particularly for identifying detailed spatial features. Additionally, success rate curves were employed to further evaluate the predictive performance. As shown in Fig. 8, the success rate curve of the C-GAT model is closer to the upper-left corner than that of the GAT model, clearly indicating its superior predictive accuracy and generalization. Specifically, C-GAT captured a higher proportion of known Li deposits within smaller prospective areas, effectively demonstrating its capability for prioritizing geologically significant exploration targets.

4.3 Robustness of C-GAT to Perturbation

To evaluate the robustness advantages of the C-GAT compared to the GAT, we applied global Gaussian noise with average intensities of 10% and 20% at the model nodes to simulate the medium- and medium-high-intensity noise, respectively, commonly encountered in geochemical survey data during sampling and other stages. This study compared the anomaly recognition results generated under different noise levels, along with the loss curves for both models under various noise perturbations.

After introducing a 10% global perturbation, C-GAT maintained (Fig. 9a) a majority of its high-anomaly-score prediction zones, with most known deposits still located within these high-anomaly areas. The overall identification results are consistent with the spatial distribution of ore-controlling rock masses and major faults in the region. In contrast, the prediction accuracy of the GAT (Fig. 9b) significantly declined under 10% noise, with many locations failing to be predicted as high-anomaly areas, showing a clear mismatch with the spatial distribution of the controlling rock masses and faults. When the noise level increased to 20%, the results from the GAT (Fig. 10b) became unreliable, with only a few concentrated known deposits accurately located in the high-anomaly zones. In contrast, the C-GAT (Fig. 10a) still demonstrated a strong ability to accurately recognize geochemical anomalies under this medium–high noise disturbance, with a substantial number of known deposits identified within high-anomaly areas, and the overall spatial configuration and distribution of high-anomaly-score areas remaining in alignment with the controlling rock masses and faults. Particularly in areas with known granite bodies, such as Wugong and North Zhuguang, C-GAT was noticeably less affected by noise, whereas GAT experienced a substantial loss of recognition performance under perturbations. This indicates that C-GAT, which incorporates causal knowledge, exhibits a stronger robustness against noise than GAT.

Similar conclusions can be drawn from different comparison indices (Fig. 11). The loss function used here to evaluate the model performance under perturbations was exactly the same as the loss function used to train the models, specifically the negative log-likelihood loss (NLL loss). This consistency ensures that the evaluation of model robustness directly reflects the model's predictive stability under noisy conditions, maintaining a fair and consistent performance comparison across different perturbation levels. In the absence of perturbations, the losses of the C-GAT and GAT models were 0.0325 and 0.0425, respectively. When the perturbation intensity increases to 10%, the loss for C-GAT only increases by approximately 0.015–0.0475, whereas the loss

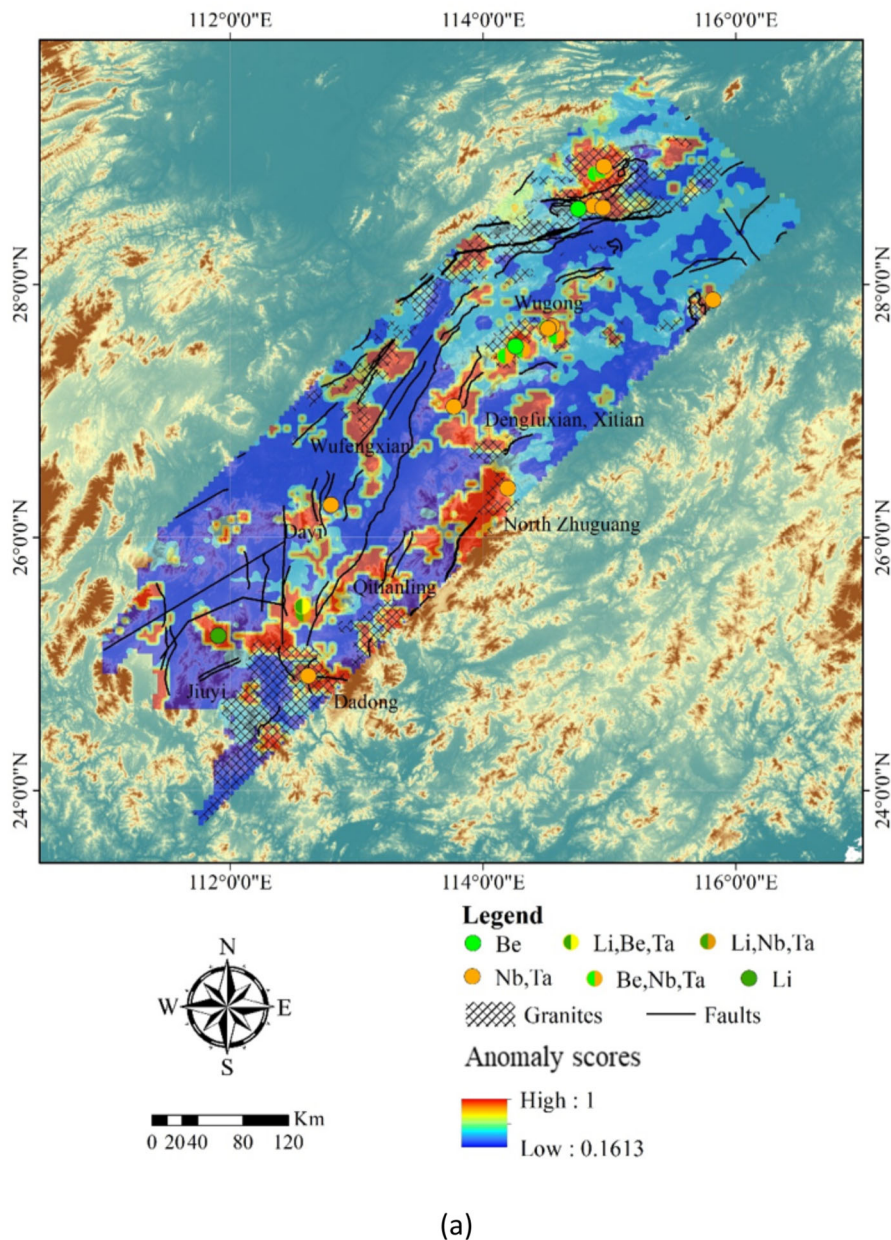


Fig. 9 Geochemical anomaly maps identified by **a** C-GAT with 10% noise level and **b** GAT with 10% noise level

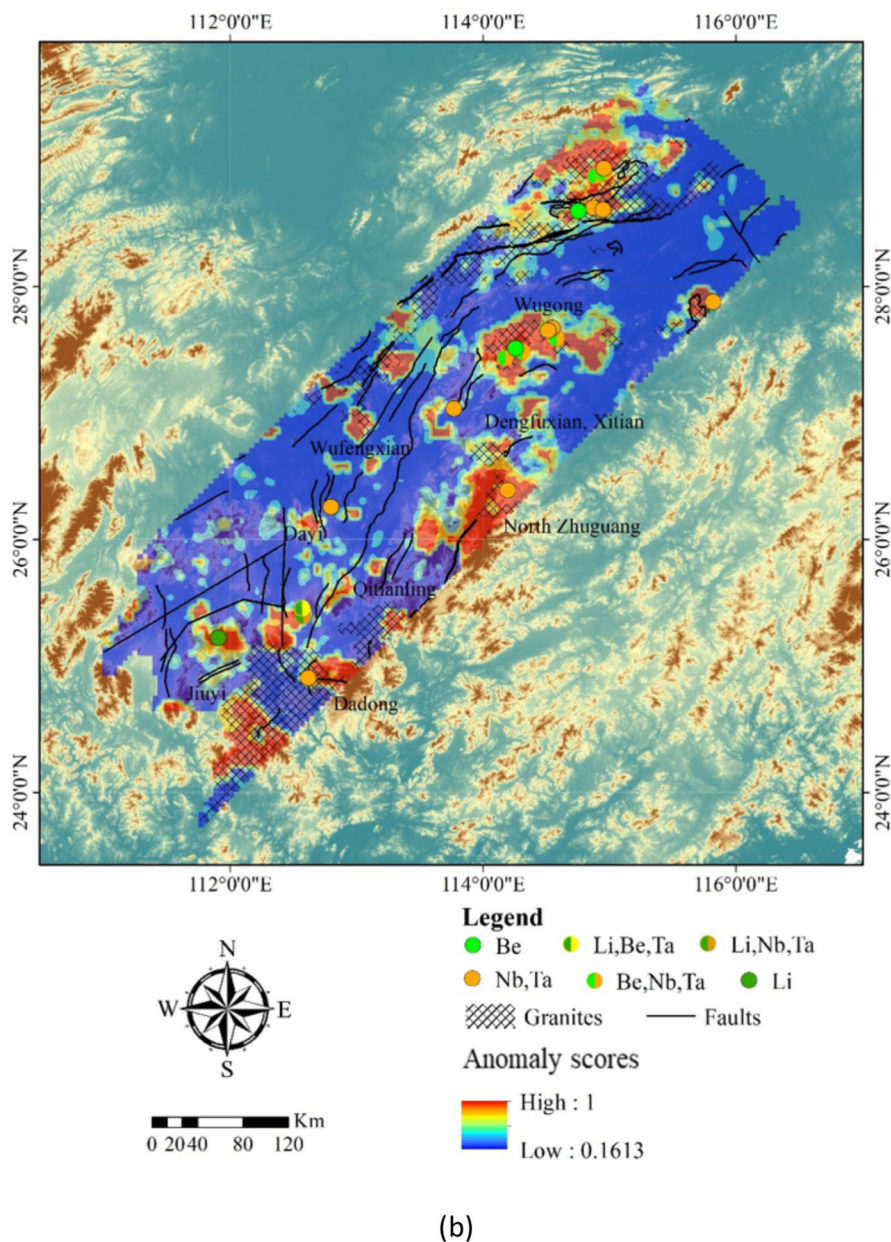


Fig. 9 continued

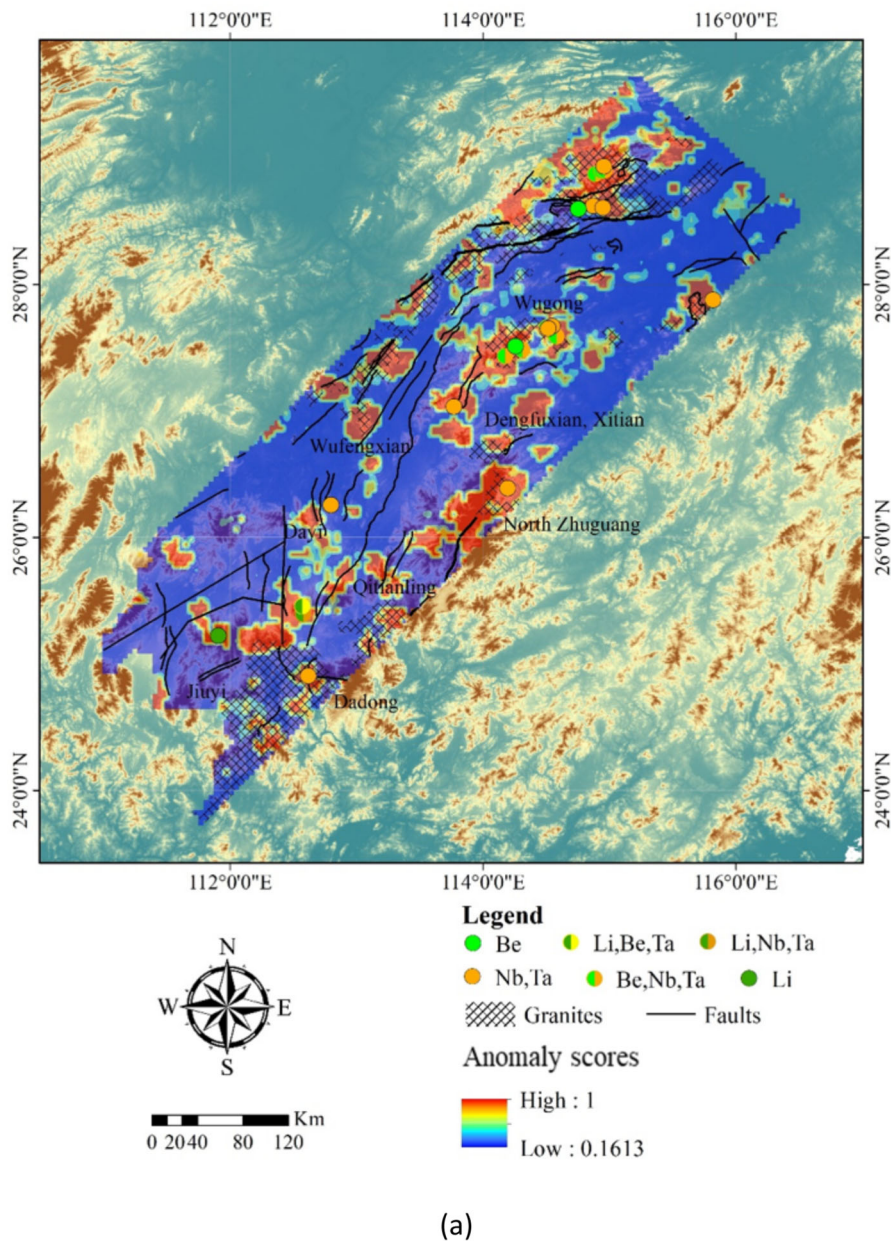


Fig. 10 Geochemical anomaly maps identified by **a** C-GAT with 20% noise level and **b** GAT with 20% noise level

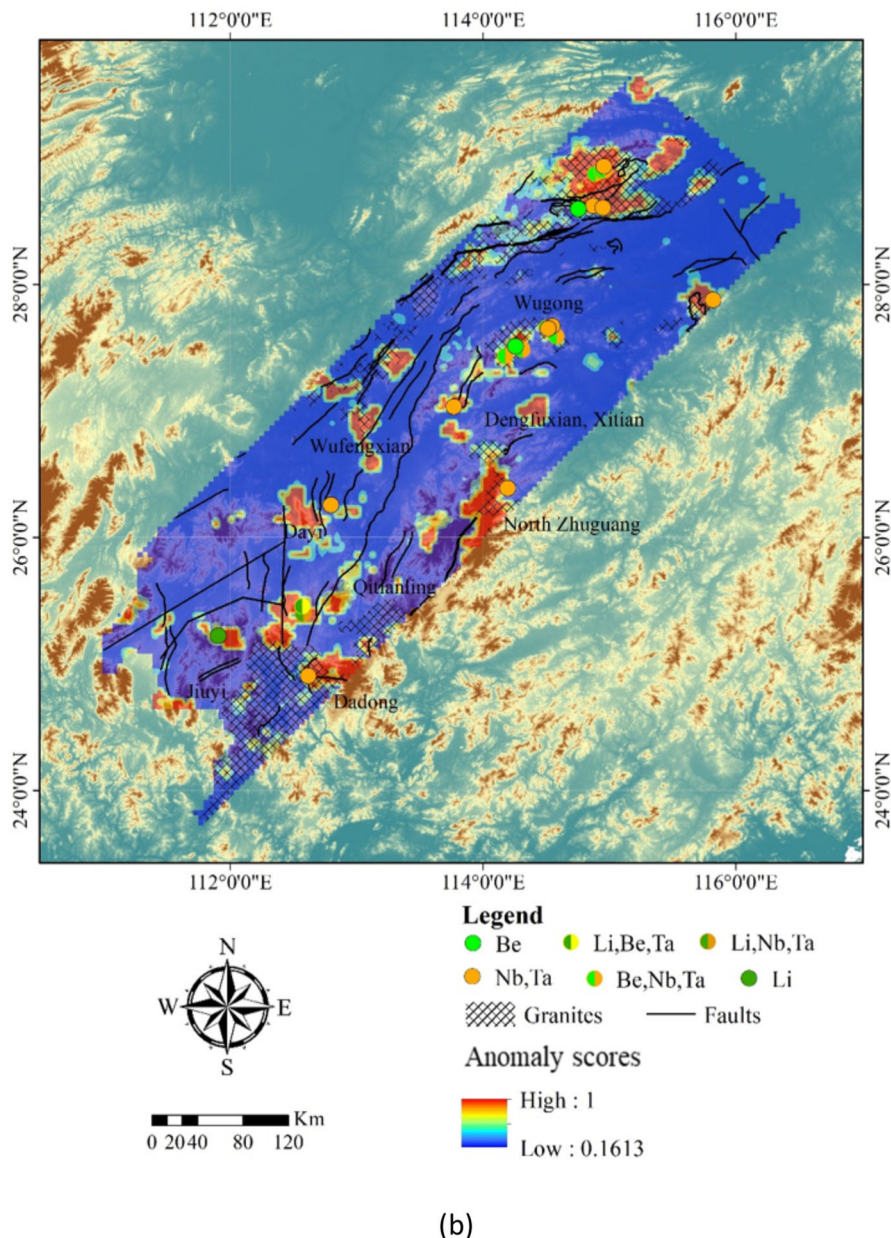


Fig. 10 continued

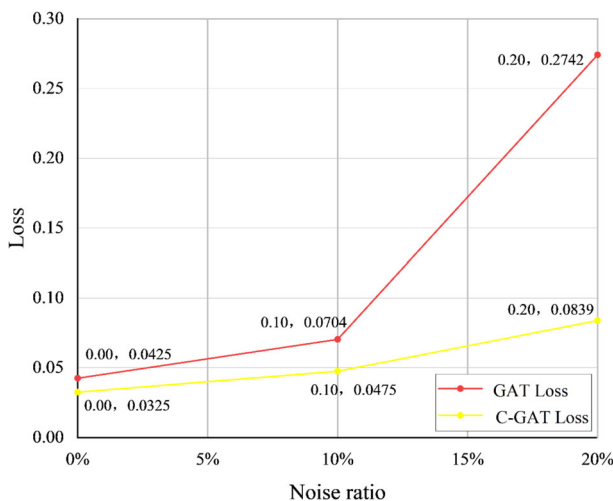


Fig. 11 Comparison of loss between C-GAT and GAT with different levels of noise

of GAT jumps significantly to 0.0704, with both the numerical value and increase being higher than those of C-GAT. When the perturbation was further increased to 20%, the loss of the GAT rapidly increased to 0.2742 (an increase of 0.2038), whereas the loss of C-GAT only increased by 0.0364–0.0839. Overall, the loss value for C-GAT outperformed that of GAT, both globally and locally, in terms of loss rates and increases in loss rates across different perturbation levels. These comparisons clearly and quantitatively illustrate that the robustness of C-GAT, including of causal knowledge, is significantly superior to that of GAT.

5 Conclusions

This study presents a hybrid model, C-GAT, which combines the causal discovery model LiNGAM with a graph attention network (GAT), demonstrating substantial improvements in the interpretability and robustness of geochemical anomaly identification. By embedding causally relevant relationships within the data structure, C-GAT effectively learns the causal relationship between geochemical variables and mineralization, which enhances the attention mechanism to prioritize critical ore-forming elements and reduces the influence of noise. The results indicate that C-GAT consistently outperforms the traditional GAT model in handling noise perturbations and achieves higher accuracy and robustness across various noise intensities. Beyond improving anomaly identification accuracy, C-GAT also shows promise for extracting geologically significant causal features from complex variable interactions, providing a more interpretable approach to mineralization analysis. Future work may focus on further integrating causal inference algorithms with graph neural networks to enhance the model's accuracy, robustness, and interpretability, particularly in the context of big data applications in geochemical exploration.

Acknowledgements This study is funded by the National Key Research and Development Program of China (no. 22023YFC2906404), the Key Research and Development Program of Xinjiang Uygur Autonomous Region, China (no. 2024B03010-3), the Natural Science Foundation of Hubei Province (China) (2023AFA001), and the MOST Special Fund from State Key Laboratory of Geological Processes and Mineral Resources, China University of Geosciences (MSFGPMR2025-401).

Data Availability The data utilized in this research are sourced from Wang et al. (2007, 2013) provided by the China Geological Survey.

Declarations

Conflict of interest The authors declare that they have no known competing financial interests or personal relationships that could have appeared to influence the work reported in this paper.

References

- Agterberg F (2014) Geomathematics: theoretical foundations, applications and future developments, vol 18. Springer, Berlin. <https://doi.org/10.1007/978-3-319-06874-9>
- Altman N, Krzywinski M (2015) Points of Significance: Association, correlation and causation. Nat Methods 12(10):899–900. <https://doi.org/10.1038/nmeth.3587>
- Carlini N, Wagner D (2017) Towards evaluating the robustness of neural networks. In: 2017 IEEE symposium on security and privacy. IEEE, pp 39–57. <https://doi.org/10.1109/sp.2017.49>
- Carranza EJM (2008) Geochemical anomaly and mineral prospectivity mapping in GIS, vol 11. Elsevier, Amsterdam. [https://doi.org/10.1016/s0168-6275\(08\)x0001-7](https://doi.org/10.1016/s0168-6275(08)x0001-7)
- Che X, Wang R, Wu F, Zhu Z, Zhang W, Hu H, Xie L, Lu J, Zhang D (2019) Episodic Nb-Ta mineralisation in South China: constraints from in situ LA-ICP-MS columbite-tantalite U-Pb dating. Ore Geol Rev 105:71–85. <https://doi.org/10.1016/j.oregeorev.2018.11.023>
- Chen J, Jahn BM (1998) Crustal evolution of southeastern China: Nd and Sr isotopic evidence. Tectono-physics 284(1–2):101–133. [https://doi.org/10.1016/s0040-1951\(97\)00186-8](https://doi.org/10.1016/s0040-1951(97)00186-8)
- Chen P, Hua R, Zhang B, Lu J, Fan C (2002) Early Yanshanian post-orogenic granitoids in the Nanling region: petrological constraints and geodynamic settings. Sci China (Ser d) 45(8):1674–7313. <https://doi.org/10.1360/02yd9076>
- Cheng Q (2012) Singularity theory and methods for mapping geochemical anomalies caused by buried sources and for predicting undiscovered mineral deposits in covered areas. J Geochem Explor 122:55–70. <https://doi.org/10.1016/j.gexplo.2012.07.007>
- Cortez P, Embrechts MJ (2013) Using sensitivity analysis and visualization techniques to open black box data mining models. Inf Sci 225:1–17. <https://doi.org/10.1016/j.ins.2012.10.039>
- Cox S (2005) Coupling between deformation, fluid pressures, and fluid flow in ore-producing hydrothermal systems at depth in the crust. Econ Geol. <https://doi.org/10.5382/av100.04>
- Geisler S, Schmidt T, Şirin H, Zügner D, Bojchevski A, Günnemann S (2021) Robustness of graph neural networks at scale. Adv Neural Inf Process Syst 34:7637–7649. <https://doi.org/10.48550/arXiv.2110.14038>
- Goodfellow I, Shlens J, Szegedy C (2014) Explaining and harnessing adversarial examples. arXiv:1412.6572. <https://doi.org/10.48550/arXiv.1412.6572>
- Gori M, Monfardini G, Scarselli F (2005) A new model for learning in graph domains. In: Proceedings. 2005 IEEE international joint conference on neural networks 2005. (2), 729–734. IEEE. <https://doi.org/10.1109/ijcnn.2005.1555942>
- Grunsky EC (2010) The interpretation of geochemical survey data. Geochem Explor Environ Anal 10(1):27–74. <https://doi.org/10.1144/1467-7873/09-210>
- Guan Q, Ren S, Chen L, Yao Y, Hu Y, Wang R, Feng B, Gu L, Chen W (2022) Recognizing multivariate geochemical anomalies related to mineralization by using deep unsupervised graph learning. Nat Resour Res 31(5):2225–2245. <https://doi.org/10.1007/s11053-022-10088-x>
- Guo R, Cheng L, Li J, Hahn P, Liu H (2020) A survey of learning causality with data: problems and methods. ACM Comput Surv 53(4):1–37. <https://doi.org/10.1145/3397269>

- Han H, Wu Y, Qin X (2021) An interactive graph attention networks model for aspect-level sentiment analysis. *J Electron Inf Technol* 43(11):3282–3290. <https://doi.org/10.11999/JEIT210036>
- Hogan A, Blomqvist E, Cochez M, d'Amato C, Melo GD, Gutierrez C, Kirrane S, Gayo JEM, Navigli R, Neumaier S, Ngomo CAN, Polleres A, Rashid SM, Rula A, Schmelzeisen L (2021) Knowledge graphs. *ACM Comput Surv* 54(4):1–37. <https://doi.org/10.1145/3447772>
- Hu W, Huang X (2005) Characteristics and genesis of pegmatite type Nb-Ta spodumene deposit in Xigang, South Jiangxi. *Resour Surv Environ* 26(4):258–266. <https://doi.org/10.3969/j.issn.1671-4814.2005.04.004>
- Hua R, Chen P, Zhang W, Yao J, Lin J, Zhang Z (2005) Metallogenesis and their geodynamic settings related to mesozoic granitoids in the nanling range. *Geol J China Univ* 11(3):291–304. <https://doi.org/10.1111/j.1755-6724.2005.tb00936.x>
- Iglesias-Suarez F, Gentile P, Solino-Fernandez B, Beucler T, Pritchard M, Runge J, Eyring V (2024) Causally-informed deep learning to improve climate models and projections. *J Geophys Res Atmosp* 129(4):039202. <https://doi.org/10.1029/2023jd039202>
- Jin Z, Zhang Y, Wu F, Zhu W, Pan Y (2023) Artificial intelligence algorithms based on data-driven and knowledge-guided models. *J Electron Inf Technol* 45(7):2580–2594. <https://doi.org/10.11999/JEIT220700>
- Kaddour J, Lynch A, Liu Q, Kusner M, Silva R (2022) Causal machine learning: a survey and open problems. [arXiv:2206.15475](https://arxiv.org/abs/2206.15475)
- Karpatne A, Atluri G, Faghmous J, Steinbach M, Banerjee A, Ganguly A, Shekhar S, Samatova N, Kumar V (2017) Theory-guided data science: a new paradigm for scientific discovery from data. *IEEE Trans Knowl Data Eng* 29(10):2318–2331. <https://doi.org/10.1109/tkde.2017.2720168>
- Kipf T, Welling M (2016) Semi-supervised classification with graph convolutional networks. [arXiv:1609.02907](https://arxiv.org/abs/1609.02907). <https://doi.org/10.48550/arXiv.1609.02907>
- Lagemann K, Lagemann C, Taschler B, Mukherjee S (2023) Deep learning of causal structures in high dimensions under data limitations. *Nat Mach Intell* 5(11):1306–1316. <https://doi.org/10.1038/s42256-023-00744-z>
- LeCun Y, Bengio Y, Hinton G (2015) Deep learning. *Nature* 521(7553):436–444. <https://doi.org/10.1038/nature14539>
- Li X, Li W, Li Z (2007) Rediscussion on genetic types and tectonic significance of early Yanshan granites in Nanling. *Chin Sci Bull* 52(9):981–992. <https://doi.org/10.1360/csb2007-52-9-981>
- Liu J, Zheng S, Wang C (2023) Causal graph attention network with disentangled representations for complex systems fault detection. *Reliab Eng Syst Saf* 235:109232. <https://doi.org/10.1016/j.ress.2023.109232>
- Liu SB, Yang Y, Wang D, Dai H, Ma S, Liu L, Wang C (2019) Discovery and significance of granite type lithium industrial orebody in Jiajika orefield, Sichuan Province. *Acta Geol Sin* 93(6):1309–1320. <https://doi.org/10.19762/j.cnki.dizhixuebao.2019184>
- Luo Y, Peng J, Ma J (2020) When causal inference meets deep learning. *Nat Mach Intell* 2(8):426–427. <https://doi.org/10.1038/s42256-020-0218-x>
- Luo Z, Zuo R, Xiong Y (2022) Visual interpretable deep learning algorithm for geochemical anomaly recognition. *Nat Resour Res* 31(5):2211–2223. <https://doi.org/10.1007/s11053-022-10080-5>
- Luo Z, Zuo R (2025) Causal discovery and deep learning algorithms for detecting geochemical patterns associated with gold-polymetallic mineralization: a case study of the Edongnan Region. *Math Geosci* 57:193–220. <https://doi.org/10.1007/s11004-024-10153-6>
- Moraffah R, Karami M, Guo R, Raglin A, Liu H (2020) Causal interpretability for machine learning-problems, methods and evaluation. *ACM SIGKDD Explor News* 22(1):18–33. <https://doi.org/10.1145/3400051.3400058>
- Mujkanovic F, Geisler S, Günemann S, Bojchevski A (2022) Are defenses for graph neural networks robust? *Adv Neural Inf Process Syst* 35:8954–8968. <https://doi.org/10.48550/arXiv.2301.13694>
- Nickel M, Murphy K, Tresp V, Gabrilovich E (2015) A review of relational machine learning for knowledge graphs. *Proc IEEE* 104(1):11–33. <https://doi.org/10.1109/jproc.2015.2483592>
- Nykanen V, Lahti I, Niiranen T, Korhonen K (2015) Receiver operating characteristics (ROC) as validation tool for prospectivity models—a magmatic Ni-Cu case study from the Central Lapland Greenstone Belt, northern Finland. *Ore Geol Rev* 71:853–860. <https://doi.org/10.1016/j.oregeorev.2014.09.007>
- Pan Y (2016) Heading toward artificial intelligence 2.0. *Engineering* 2(4):409–413. <https://doi.org/10.1016/j.eng.2016.04.018>

- Pearl J (2000) Models, reasoning and inference, vol 19(2). Cambridge University Press, Cambridge, p 3. <https://doi.org/10.1007/bf02294851>
- Pearl J (2010) An introduction to causal inference. *Int J Biostat* 6:2. <https://doi.org/10.2202/1557-4679.1203>
- Pei T, Bao Z (1998) Study on geochemical data denoising methods. *Geol Geochem* 04:86–90
- Peters J, Janzing D, Schölkopf B (2017) Elements of causal inference: foundations and learning algorithms. The MIT Press, Cambridge, p 288
- Qiao G, Zhang H, Wu Y, Jin M, Du W, Zhao X, Chen D (2015) Petrogenesis of the Dahongliutan monzogranite in western Kunlun: constraints from SHRIMP zircon U-Pb geochronology and geochemical characteristics. *Acta Geol Sin* 89(7):1180–1194. <https://doi.org/10.3969/j.issn.0001-5717.2015.07.003>
- Raiissi M, Perdikaris P, Karniadakis GE (2019) Physics-informed neural networks: a deep learning framework for solving forward and inverse problems involving nonlinear partial differential equations. *J Comput Phys* 378:686–707. <https://doi.org/10.1016/j.jcp.2018.10.045>
- Reichstein M, Camps-Valls G, Stevens B, Jung M, Denzler J, Carvalhais N, Prabhat F (2019) Deep learning and process understanding for data-driven Earth system science. *Nature* 566(7743):195–204. <https://doi.org/10.5194/egusphere-egu24-15874>
- Runge J, Bathiany S, Bollt E, Camps-Valls G, Coumou D, Deyle E, Zscheischler J (2019) Inferring causation from time series in Earth system sciences. *Nat Commun* 10(1):2553. <https://doi.org/10.1038/s41467-019-10105-3>
- Schölkopf B (2022) Causality for machine learning. In: Probabilistic and causal inference: the works of Judea Pearl, pp 765–804. <https://doi.org/10.1145/3501714.3501755>
- Schölkopf B, Locatello F, Bauer S, Ke N, Kalchbrenner N, Goyal A, Bengio Y (2021) Toward causal representation learning. *Proc IEEE* 109(5):612–634. <https://doi.org/10.1109/jproc.2021.3058954>
- Shimizu S, Hoyer P, Hyvärinen A, Kerminen A, Jordan M (2006) A linear non-Gaussian acyclic model for causal discovery. *J Mach Learn Res* 7(10):2003–2030
- Shimizu S (2014) LiNGAM: non-Gaussian methods for estimating causal structures. *Behaviormetrika* 41(1):65–98. <https://doi.org/10.2333/bhmk.41.65>
- Sloman SA, Lagnado D (2015) Causality in thought. *Annu Rev Psychol* 66(1):223–247. <https://doi.org/10.1146/annurev-psych-010814-015135>
- Sui Y, Wang X, Wu J, Chua TS (2022) Causal attention for interpretable and generalizable graph classification. In: Proceedings of the 28th ACM SIGKDD conference on knowledge discovery and data mining, pp 1696–1705. <https://doi.org/10.1145/3534678.3539366>
- Tesch T, Kollet S, Garcke J (2023) Causal deep learning models for studying the Earth system. *Geosci Model Dev* 16(8):2149–2166. <https://doi.org/10.5194/gmd-16-2149-2023>
- Tobler W (1970) A computer movie simulating urban growth in the detroit region. *Econ Geogr*. <https://doi.org/10.2307/143141>
- Veličković P, Cucurull G, Casanova A, Romero A, Lio P, Bengio Y (2018) Graph attention networks arXiv: 1710.10903. <https://doi.org/10.48550/arXiv.1710.10903>
- Wang C, Wang M, Wang B, Chen J, Ma X, Jiang S (2024a) Knowledge graph-infused quantitative mineral resource forecasting. *Earth Sci Front* 31(4):026–036. <https://doi.org/10.13745/j.esf.sf.2024.5.3>
- Wang D, Shen W (2003) The genesis of granites and crustal evolution in southeastern China. *Earth Sci Front* 10(3):209–220. <https://doi.org/10.3321/j.issn:1005-2321.2003.03.020>
- Wang L, Huang S, Wang S, Liao J, Li T, Liu L (2024b) A survey of causal discovery based on functional causal model. *Eng Appl Artif Intell* 133:108258. <https://doi.org/10.1016/j.engappai.2024.108258>
- Wang X, Zhang Q, Zhou G (2007) National-scale geochemical mapping projects in China. *Geostand Geoanal Res* 31(4):311–320. <https://doi.org/10.1111/j.1751-908X.2007.00128.x>
- Wang X, Xu S, Chi Q, Liu X, Wang W (2013) Mass accumulation and distribution of metallogenetic elements in the South China block. *Geochimica* 42(3):229–241. <https://doi.org/10.3969/j.issn.0379-1726.2013.03.005>
- Wang Z, Shen H, Cao Q, Cheng X (2022) A survey on graph classification research. *J Softw* 01:171–192. <https://doi.org/10.13328/j.cnki.jos.006323>
- Wen C, Shao Y, Huang G, Luo X, Li S (2017) Geochemical features and mineralization of Jianfengling rare metal granite in Hunan Province. *Mineral Deposits* 36(4):879–892. <https://doi.org/10.16111/j.0258-7106.2017.04.006>

- Wen C, Shao Y, Xiong Y, Li J, Jiang S (2021) Ore genesis of the Baishawo Be-Li-Nb-Ta deposit in the northeast Hunan Province, south China: evidence from geological, geochemical, and U-Pb and Re-Os geochronologic data. *Ore Geol Rev* 129:10389510. <https://doi.org/10.1016/j.oregeorev.2020.103895>
- Wessels H, Weißenfels C, Wrighers P (2020) The neural particle method—an updated Lagrangian physics informed neural network for computational fluid dynamics. *Comput Methods Appl Mech Eng* 368:113127. <https://doi.org/10.1016/j.cma.2020.113127>
- Xie X, Mu X, Ren T (1997) Geochemical mapping in China. *J Geochem Explor* 60:99–113. [https://doi.org/10.1016/s0375-6742\(97\)00029-0](https://doi.org/10.1016/s0375-6742(97)00029-0)
- Xi X, Li M (2017) Summary of modern exploration geochemistry scientific system: commentary on exploration achievements obtained in the period of 12th Five-Year Plan. *Geophys Geochem Explor* 41:779–793. <https://doi.org/10.11720/wtyht.2017.5.01>
- Xiong Y, Zuo R (2016) Recognition of geochemical anomalies using a deep autoencoder network. *Comput Geosci* 86:75–82. <https://doi.org/10.1016/j.cageo.2015.10.006>
- Xiong Y, Zuo R, Carranza EJM (2018) Mapping mineral prospectivity through big data analytics and a deep learning algorithm. *Ore Geol Rev* 102:811–817. <https://doi.org/10.1016/j.oregeorev.2018.10.006>
- Xiong Y, Zuo R (2021) Robust feature extraction for geochemical anomaly recognition using a stacked convolutional denoising autoencoder. *Math Geosci* 54:623–644. <https://doi.org/10.1007/s11004-021-09935-z>
- Xiong Y, Zuo R, Luo Z, Wang X (2022) A physically constrained variational autoencoder for geochemical pattern recognition. *Math Geosci* 54:783–806. <https://doi.org/10.1007/s11004-021-09979-1>
- Xiong Y, Zuo R, Miller SA (2023) The behavior of hydrothermal mineralization with spatial variations of fluid pressure. *J Geophys Res Solid Earth* 128(2):e2022JB025255. <https://doi.org/10.1029/2022jb025255>
- Xu Y, Zuo R, Zhang G (2023) The graph attention network and its post-hoc explanation for recognizing mineralization-related geochemical anomalies. *Appl Geochem* 155:105722. <https://doi.org/10.1016/j.apgeochem.2023.105722>
- Xu Z, Wang R, Zhao Z, Fu X (2018) On the structural backgrounds of the large-scale “hard-rock type” lithium ore belts in China. *Acta Geol Sin* 92(6):1091–1106. <https://doi.org/10.3969/j.issn.0001-5717.2018.06.001>
- Xuan Y, Yuan S, Yuan Y (2014) Preliminary comparative studies on the metallogenesis of two types of Pb-Zn-polymetallic deposits in Huangshaping-Baoshan area, Southern Hunan Province, China. *Acta Geol Sin (Engl Ed)* 88:54–55. https://doi.org/10.1111/1755-6724.12367_26
- Yan Q, Xue L, Li Y, Wang R, Wu B, Ding WJ (2023) Mineral prospectivity mapping integrated with geological map knowledge graph and geochemical data: a case study of gold deposits at Raofeng area, Shaanxi Province. *Ore Geol Rev* 161:105651. <https://doi.org/10.1016/j.oregeorev.2023.105651>
- Yan Q, Zhao J, Xue L, Wei L, Ji M, Ran X, Dai J (2024) Mineral prospectivity mapping based on spatial feature classification with geological map knowledge graph embedding: case study of gold ore prediction at Wulonggou, Qinghai Province (Western China). *Nat Resour Res* 33:2385–2406. <https://doi.org/10.1007/s11053-024-10386-6>
- Yang M, Mei Y (1997) Characteristics of geology and metallization in the Qinzhou-Hangzhou paleoplatform juncture. *Geol Miner Resour South China* 3:52–59
- Zhang T, Cheng Y, Sun X (2023) Graph attention network based on causal inference. *Comput Sci* 1:157–165. <https://doi.org/10.11896/jsjxkz.220600230>
- Zhang Y, Dong S, Li J, Cui J, Shi W, Su J, Li Y (2012) New advances in Mesozoic tectonic studies of South China. *Acta Geosci Sin* 03:257–279. <https://doi.org/10.3975/cagsb.2012.03.01>
- Zhao Z, Chen Y, Wang D, Li J, Liu S, Chen Z, Wang P (2022) Superimposed evolution of Mesozoic tectonic regime transformation and tungsten-tin-lithium-beryllium-niobium-tantalum-rare earth mineralization series in South China. *Acta Petro Sin* 02:301–322. <https://doi.org/10.18654/1000-0569/2022.02.01>
- Zhou X, Sun T, Shen W (2006) Petrogenesis of Mesozoic granitoids and volcanic rocks in South China: a response to tectonic evolution. *Episodes* 29:26–33. <https://doi.org/10.18814/epiugs/2006/v29i1/004>
- Zuo R (2016) A nonlinear controlling function of geological features on magmatic-hydrothermal mineralization. *Sci Rep* 6(1):27127. <https://doi.org/10.1038/srep27127>
- Zuo R, Xiong Y (2018) Big data analytics of identifying geochemical anomalies supported by machine learning methods. *Nat Resour Res* 27:5–13. <https://doi.org/10.1007/s11053-017-9357-0>
- Zuo R, Xiong Y, Wang J, Carranza EJM (2019) Deep learning and its application in geochemical mapping. *Earth Sci Rev* 192:1–14. <https://doi.org/10.1016/j.earscirev.2019.02.023>

- Zuo R, Wang J, Xiong Y, Wang Z (2021) The processing methods of geochemical exploration data: past, present, and future. *Appl Geochem* 132:105072. <https://doi.org/10.1016/j.apgeochem.2021.105072>
- Zuo R, Xiong Y, Wang Z, Wang J, Kreuzer OP (2023) A new generation of artificial intelligence algorithms for mineral prospectivity mapping. *Nat Resour Res* 32(5):1859–1869. <https://doi.org/10.1007/s11053-023-10237-w>
- Zuo R, Cheng Q, Xu Y, Yang F, Xiong Y, Wang Z, Kreuzer OP (2024) Explainable artificial intelligence models for mineral prospectivity mapping. *Sci China Earth Sci* 67(9):2864–2875. <https://doi.org/10.1007/s11430-024-1309-9>

Springer Nature or its licensor (e.g. a society or other partner) holds exclusive rights to this article under a publishing agreement with the author(s) or other rightsholder(s); author self-archiving of the accepted manuscript version of this article is solely governed by the terms of such publishing agreement and applicable law.